Journal of Metals, Materials and Minerals, Vol. 33, No. 1, pp. 27-38, 2023

Corrosion of a spark plasma sintered Fe-Cr-Mo-B-C alloy in 3.5% NaCl solution

Mudassir FAROOQ[1,3,*], Sohail MUHAMMAD[3], and A. A. SOROUR[1,2,*]

1 Department of Mechanical Engineering, King Fahd University of Petroleum & Minerals (KFUPM), Dhahran 31261, Saudi Arabia
2 Interdisciplinary Research Center for Advanced Materials, King Fahd University of Petroleum & Minerals (KFUPM), Dhahran 31261, Saudi Arabia
3 Department of Materials Engineering, NED University of Engineering and Technology, Karachi 75270, Pakistan

***Corresponding author e-mail:** mudassir@neduet.edu.pk

Received date:
20 June 2022
Revised date
16 November 2022
Accepted date:
28 December 2022

Keywords:
Corrosion;
Powder metallurgy;
Amorphous alloy powder;
Passive film

Abstract

In this study, the corrosion behavior of a Fe-Cr-Mo-B-C alloy, fabricated by spark plasma sintering of an amorphous alloy powder, in 3.5% NaCl solution was analyzed. Electrochemical impedance spectroscopy and potentiodynamic polarization are techniques which were used for electrochemical performance estimation of samples and the results were further compared with conventional alloys: 1080 carbon steel and 304 stainless steel. Corrosion surface products were characterized through Scanning electron microscopy, Energy dispersive x-ray spectroscopy and X-ray photoelectron spectroscopy. Specimens sintered at 800°C (S1-800) had achieved 94% densification approximately while the sample sintered at 900°C (S2-900), had densified more which was 98% approximately. S2-900 had better corrosion resistance than S1-800 while in comparison to conventional alloys; it was inferior to 304 stainless steel. It was concluded that the increase in density of sintered samples favoured the formation of more uniform surface products and enhanced the formation of the passive chromium oxide (Cr_2O_3) layer.

1. Introduction

Amorphous metals is relatively a new approach in metal's research and their unique microstructural characteristics attracted much attention in previous the decade. Fe-Cr-Mo based amorphous alloys are a good replacement of currently used stainless steel alloys because of their good corrosion resistance along with higher hardness and wear resistance [1-10] specially in reducing chloride environment. J. Jayaraj *et al*. [11] reported the formation of a stable passive region, even in higher concentration of HCl. Some major drawbacks of bulk metallic glasses include their critical thickness, low ductility and specialized techniques for their production [12-16].

It was reported that nano-crystallization has not a pronounced effect on the corrosion resistance properties of metallic glass [17,18] while control nano-crystallization improves mechanical [19-23] as well as magnetic properties [24]. Also, the effect of nano-crystallization on corrosion performance depends on surface reaction and may favor the formation of a stable passive film [25,26].

In this study, the corrosion resistance performance and its mechanism of nano-crystalline Fe-Cr-Mo-B-C alloy, fabricated from spark plasma sintering (SPS) technique, was studied in 3.5% NaCl solution. An amorphous Fe-Cr-Mo-B-C alloy powder was consolidated at 800°C and 900°C temperature. SPS is an effective pressure-assist sintering technique which provides a well-control on grain size and has the ability to preserve microstructural features very close to the initial powder with high bulk density. The electric pulse of high current intensity was used as a heating source for a limited period in the presence of uni-axial force [27,28]. The sintered samples showed the best results in terms of microstructure and corrosion performance in 1 M HCl solution, which were published [29]. The hydrochloric acid solution is a reducing environment and does not favor the formation of the strong passive film while the 3.5% NaCl solution is a neutral environment and favors the formation of a resistive oxide layer. The corrosion performance of the sintered samples was analyzed using electrochemical impedance spectroscopy (EIS) and potentiodynamic polarization (PDP) [30,31] techniques while the corrosion mechanism was studied by using scanning electron microscope (SEM) and x-ray photoelectron spectroscopy (XPS).

2. Experimental procedure

2.1 Spark plasma sintered samples

Spark Plasma Sintered (SPS) samples that contain Fe, Cr, Mo, C and B as major elements in the composition listed in Table 1, were taken for corrosion studies. The sintered density of the samples were around 94% and 98% of theoretical density of the samples with sintering temperatures of 800°C and 900°C, respectively, whereas the microstructure was consisted of $(Cr,Fe)_2B$ and $(Fe,Cr)_{23}C_6$ particles which were embedded in the Fe-based body-centered-cubic matrix [29].

Table 1. Composition of initial amorphous powder.

Elements	Fe	Cr	Mo	C	B	Others
Composition (at%)	Balance	23-25	8-10	8-8.5	8.7-9.2	4 max.

Table 2. Nomenclature of samples.

Sample name	Description	Purpose
S1-800	SPS sintered samples at 800°C	Main study
S2-900	SPS sintered samples at 900°C	Main study
S.S-304	Austenitic stainless steel, AISI-304	Reference for comparison
CS-1080	Carbon steel, AISI-1080	Reference for comparison

2.2 Corrosion testing

The sample preparation for electrochemical analysis was started by soldering a copper wire to the samples and subsequently mounting them into resin through the cold mounting process. After mounting, they were ground up-to 600-mesh paper followed by washing with ethanol and distilled water and then dried by hot air. In addition to the two sintered samples, austenitic stainless steel (S.S-304) and carbon steel (CS-1080) samples were also used for comparison. The nomenclature is listed in Table 2. The exposed sample area of 0.2 cm^2 was used for all experiments. Three cell electrode apparatus by "Gamry-3000TM" was used to perform electrochemical studies using a 3.5% NaCl solution. Ag/AgCl electrode is used as a reference while the counter electrode is of graphite. The open-circuit delay is 1 h for EIS measurement. The samples were analyzed in the frequency range of 100 mHz to 1 × 10^5 Hz while the applied AC voltage was 10 mV. PDP tests were measured with a scanning rate of 0.5 $mV{\cdot}s^{-1}$ in an applied potential range of -300 mV to +800 mV with reference to E_{corr}. The Tafel extrapolation method was used to calculate the corrosion rate from PDP data. Each test was repeated three times in order to validate the results. The immersion test was continued for 27 h in 3.5% NaCl solution to allow the formation of equilibrium corrosion products and/or oxides. After that, the samples were removed and washed with deionized water followed by hot air drying. The dried samples were then immediately characterized using SEM, EDS, and XPS.

3. Results and discussion

3.1 Corrosion performance

To determine the formation of passive film and its stability, electrochemical impedance spectroscopy test was conducted. Figure 1 shows the Nyquist plot of all tested samples in 3.5% NaCl solution. It was found that all samples formed a single distorted capacitive arc with one time constant and have mixed resistive and capacitive behavior. Also, it was found that S.S-304 formed a straight line, representing its extraordinary high charge transfer resistance. The remaining samples formed a semicircle from which the diameter of S2-900's semi-circle was greatest, followed by S1-800 and CS-1080. The diameter of the Nyquist plot semicircle has a direct relation with the charge transfer resistance of a material, whereas this relation is inverse with the corrosion rate [29].

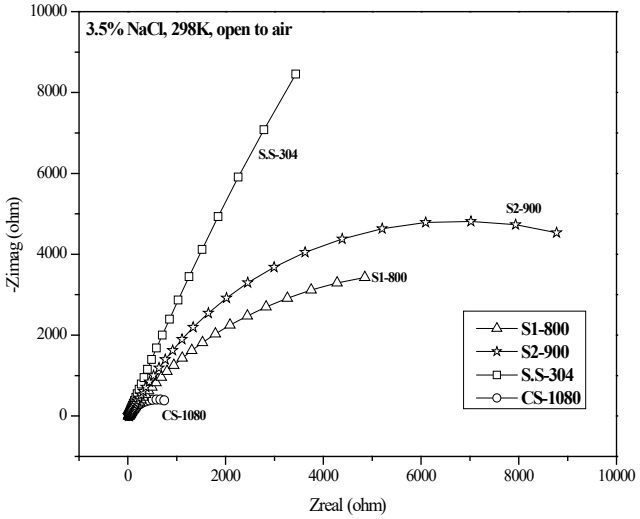

Figure 1. Nyquist Plot of all tested samples in 3.5% NaCl solution at room temperature and open to the air.

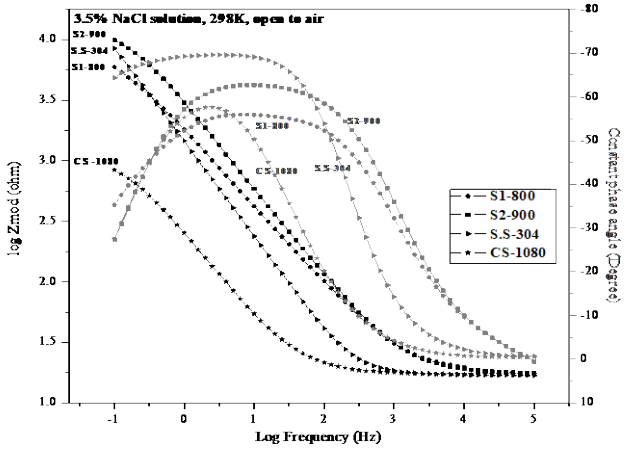

Figure 2. Frequency Vs. Impedance and Constant phase angle Bode curve of all tested samples in 3.5% NaCl solution at room temperature and open to the air.

Figure 2 shows the frequency of Impedance and constant phase angle Bode curves of all samples tested in 3.5% NaCl solution. The S2-900 showed the highest impedance value in the low-frequency region while the impedance value of S.S-304 was very near to S2-900 in the same region. It was found that the impedance value of S2-800 was lower than S.S-304 but higher than CS-1080.

With respect to constant phase angle values in Figure 2, it was found that S.S-304 has the most negative constant phase angle value which is around -70˚ in the lower frequency region. The sintered sample, S2-900, indicated a more negative constant phase angle of -63º value in comparison with S1-800, which was around -55º. The lowest negative constant phase angle value of CS-1080 was around -57º at the lower frequency region. Furthermore, the flattening of the S.S-304 curve in a wide frequency range (i.e., 31- 0.15 Hz) of the lower frequency region represents the capacitive behavior of material and evidence of high resistance in exposed solution. It was noted that both sintered samples showed a stable capacitive behavior with a wide frequency range. It was found that the capacitive behavior at frequency range for S1-800 was 100 Hz to 0.79 Hz while the same region of S2-900 was in 125 Hz to 1.2 Hz frequency range. Also, it was found that CS-1080 showed capacitive behavior but in a narrow frequency range which was 5 Hz to 1.0 Hz.

A Randel equivalent circuit was used for fitting experimental data. In this circuit, "R_{ct}" is a charge transfer resistance or polarization resistance of the material, "R_s" is a solution resistance, "CPE" is a constant phase element used instead of the pure capacitor to minimize the surface roughness and irregularities effects while "n" is an exponent which represents material behavior. The data obtained by fitting the discussed circuit showed the magnitude of "CPE" instead of capacitance. The impedance value (Z_{CPE}) can be calculated by using Equation (1) [32].

$$Z_{CPE} = Y_o^{1} \times (j\omega)^{-n} \quad (1)$$

where Y_o is the magnitude of "CPE", "ω" is the angular frequency in rad·s^{-1}, "n" is the "CPE" exponent and "j" is the imaginary unit.

The value of "Y_o" is not expressing double layer capacitance (F·cm^{-2}). The exact value of capacitance can be calculated by using Equation (2) [32].

$$C_{dl} = Y_o \, \omega_{max}^{(n-1)} \quad (2)$$

Where ω_{max} is an angular frequency in rad·s^{-1} at maximum "$-Z_{img}$".

The passive layer thickness was calculated by using Equation (3) and Equation (4) [30].

$$C = -(\omega \times -Z_{img})^{-1} \quad (3)$$

$$d_{ox} = \frac{\varepsilon_o \times \varepsilon \times A_s}{C} \quad (4)$$

where "C" is the capacitance, "$-Z_{img}$" is an imaginary impedance value at 1 kHz frequency, "ε_o" is the permittivity of free space having a value 8.85 × 10^{-14} F·cm^{-2}, "d_{ox}" is the double layer thickness, "ε" is the permittivity of di-electric which is chromium oxide (Cr_2O_3) having the value "12" and "A_s" is the exposed surface area of the electrode.

The results obtained by fitting a modified Randel model to resultant EIS data and the calculated film thickness value are shown in Table 3. According to "R_{ct}" value, S.S-304 exhibits the higher corrosion resistance and CS-1080 was lowest among all tested samples while sintered samples were between S.S-304 and CS-1080. It was found that S2-900 has higher charge transfer resistance than S1-800. With respect to passive layer thickness, the layer thickness of sintered samples was almost the same and exceeded the layer thickness on S.S-304.

Potentiodynamic polarization curves of all samples tested in 3.5% NaCl solution are shown in Figure 3. It was observed that the S.S-304 sample was spontaneously passivated with a large passive region which represents the formation of stable passive film over the substrate. Furthermore, S.S-304 showed a transformation to the trans-passive region at 0.2 V potential which is also a pitting potential of this sample. A change in slope was also noted at 0.25 V potential, but this region is not stable and represents a formation of partially passive film over the substrate.

It was also found that S1-800 did not show any active-passive transformation while S2-900 showed evidence of spontaneous passivation, but due to the absence of a stable passive region, this passive layer has limited protection. CS-1080 did not show any evidence of active-passive transformation which is an expecting behavior of carbon steel.

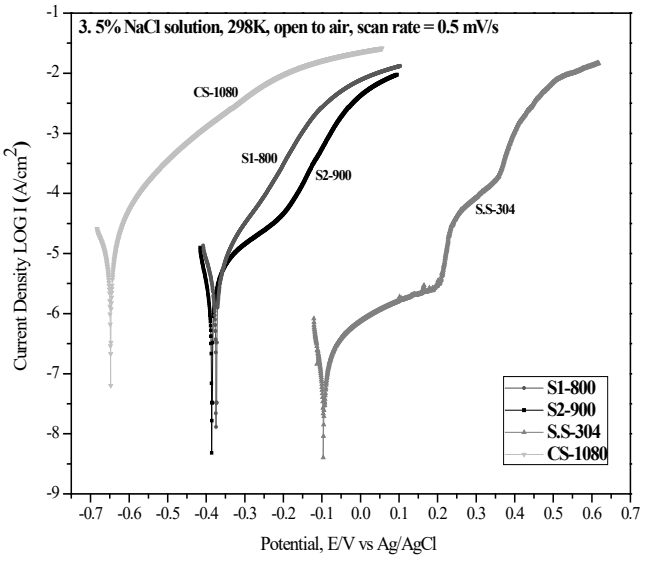

Figure 3. Potentiodynamic polarization curve of all tested samples in 3.5% NaCl solution at room temperature and open to the air.

Table 3. Shows summarize EIS results of all sample in 3.5% NaCl solution.

Material	R_{ct} (kohm.cm^{-2})	R_s (ohm.cm^{-2})	C_{dl} (µF·cm^{-2})	n	Passive layer thickness Å
S1-800	11 ± 2.00	17 ± 0.30	174 ± 0.30	0.64 ± 0.02	3 ± 0.60
S2-900	15 ± 0.26	18 ± 0.56	63 ± 23.50	0.76 ± 0.02	3 ± 0.40
S.S-304	50 ± 9.00	16 ± 0.04	164 ± 3.00	0.82 ± 0.05	2 ± 0.10
CS-1080	1 ± 0.20	17 ± 0.03	908 ± 2.50	0.77 ± 0.01	No passive film

Table 4. shows Tafel analysis summary of Potentiodynamic Polarization curves.

Material	E_{corr} (mV)	I_{corr} ($A \cdot cm^{-2}$)	Corrosion rate (mm/year)
S1-800	-(380.00 ± 6.00)	3.92 ± 0.13 µA	0.24 ± 0.01
S2-900	-(378.50 ± 7.50)	2.65 ± 0.14 µA	0.16 ± 0.01
S.S-304	-(95.70 ± 4.00)	135 ± 0.11 nA	0.02 ± 0.01
CS-1080	-(648.05 ± 2.50)	37.20 ± 0.18 µA	0.54 ± 0.13

The potentiodynamic polarization curves of all samples were further analyzed by using the Tafel extrapolation method. The summary of the results is shown in Table 4**.** It is observed from the E_{corr} value that the sintered samples are anodic to stainless steel while cathodic to carbon steel samples. It is also observed that the E_{corr} value of both sintered samples is almost similar. Furthermore, the I_{corr} value and the corrosion rate of sintered samples are greater than the stainless steel while it is less than the carbon steel sample. Moreover, the corrosion resistance performance of the S2-900 is better than the S1-800 sample.

From electrochemical testing results, it can be concluded that the corrosion resistance performance of sintered samples was inferior to the stainless steel sample. The reason for this weak performance of the sintered sample is the formation of stable chromium carbide $(Fe,Cr)_{23}C_6$ and boride $(Cr,Fe)_2B$ phases which decrease the quantity of chromium that is dissolved in the solid-solid solution of Fe-based body-centered cubic matrix. The chromium available in the form of intermetallic compounds/phases is not beneficial in the formation of passive oxide; for example, the sensitization of stainless steel. The corrosion resistance performance of chromium-containing alloy increases with the amount of chromium, dissolved in the solid-solid solution phase because only the dissolved chromium takes part in the formation of the passive chromium oxide layer which provides protection to base metal against the action of corrosive ions. Furthermore, the sintered metal/alloy usually has inferior corrosion resistance in comparison to cast metal/alloy of the same composition due to the presence of surface porosity which initiates crevice corrosion and also, hinders the formation of the uniform passive film.

3.2 Corrosion behavior

Figure 4 shows the SEM-SE images of S1-800 at different magnifications before exposure to a 3.5% NaCl solution. At low magnification as shown in Figure 4(a), it is observed that the particles having round shapes were consolidated together. However, a reasonable amount of surface porosity is also present in S1-800 sample. Figure 4(b) is the high magnification image of grain showing the nucleation of the second phases; chromium carbide (Fe,Cr)23C6 and boride (Cr,Fe)2B as explained in our published work [29].

The EDX mapping analysis of the S1-800 sample before exposure to 3.5% NaCl solution was shown in Figure 5. From Figure 5(b-d), it is observed that the main alloying elements; iron, chromium, and molybdenum are well distributed in the sintered sample. In Figure 5(e-f), it is observed that carbon and boron are available at certain specific points. The distribution of carbon and boron represented the formation of intermetallic carbide and boride phases in the sintered sample which was further confirmed with BSE and XRD analysis as available in published work [29].

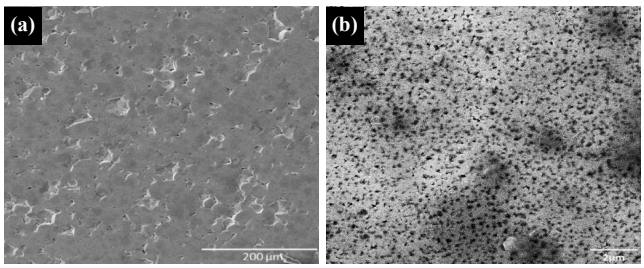

Figure 4. SEM-SE images of S1-800 before exposing to 3.5% NaCl solution etched with 1 HCl : 3 HNO_3

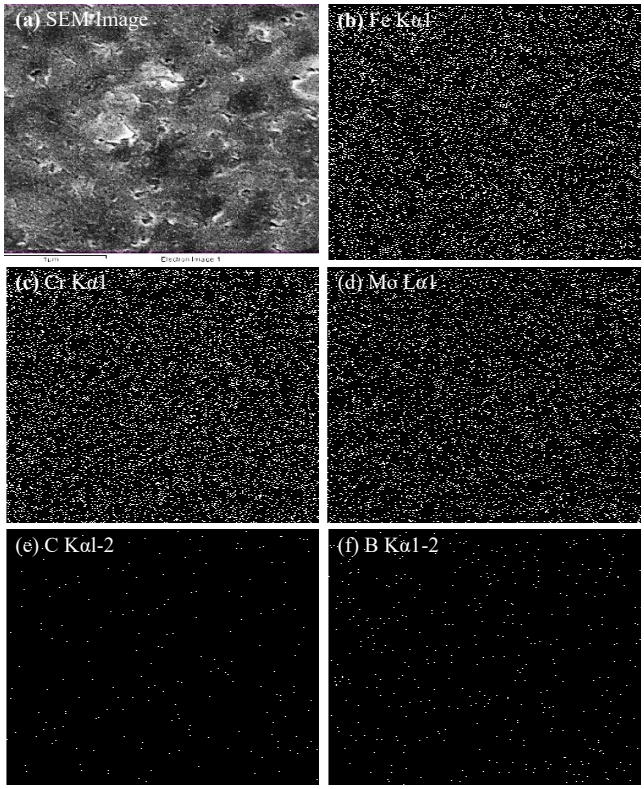

Figure 5. EDX-mapping analysis of S1-800 before exposing to a 3.5%NaCl solution.

SEM-SE images of S1-800 samples after exposure to 3.5% NaCl solution for 27 h were shown in Figure 6. In Figure 6(a), it is observed that corrosion products were formed at some specific points and not on the whole surface. Hence the surface products were non-uniformly distributed over the surface of the sample. From Figure 6(b-c), it was found that surface products have flake/wire-like morphology and agglomeration of these surface products was also witnessed at some locations. Figure 6(d) shows that the size of these flakes/wires was in nano-sized dimensions in the range of 100 nm to 200 nm.

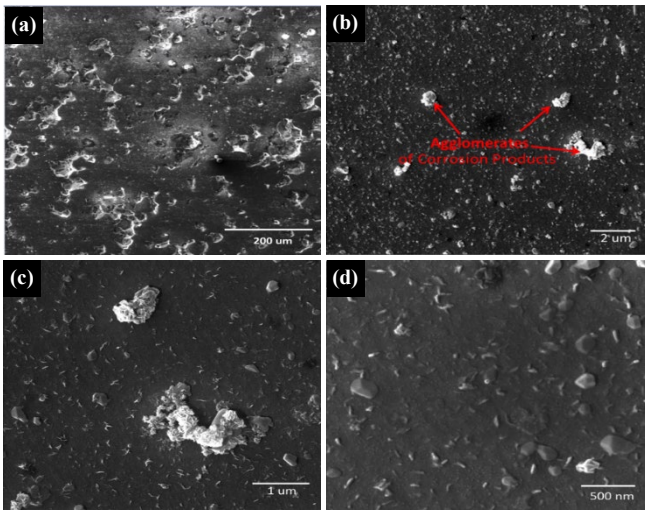

Figure 6. SEM-SE images of S1-800 after exposing to 3.5% NaCl solution for 27 h.

Figure 7 shows the EDS-mapping analysis of S1-800 after exposing it to 3.5% NaCl solution for 27 h. It was found that the concentration and distribution of sodium and chlorine bear a resemblance to each other which gave the idea that these elements were deposited as a chemical compound on the sample surface. A small amount of chlorine was also observed at sodium deficient areas which indicated that chlorine was also forming a secondary product with other alloying elements, but the amount was small. Main alloying elements like Iron (Fe), Chromium (Cr) and Molybdenum (Mo) were presented in the form of uniform distribution in the sample.

Figure 8 is the SEM-SE image of S2-900 at different magnifications before exposure to a 3.5% NaCl solution. From Figure 8(a), it is observed that the sample is well sintered, forming an almost smooth surface with some surface irregularities. In comparison to the S1-800 sample, no powder particle boundaries were observed. The powder particles are completely fused together and form a uniform material. In Figure 8(b), it is observed that the second phases such as chromium carbide $(Fe,Cr)_{23}C_6$ and boride $(Cr,Fe)_2B$, were nucleated in the S2-900 sample.

The distribution of alloying elements in S2-900 sintered samples was shown in Figure 9. From Figure 9 (b-d), it is observed that Iron, chromium, and molybdenum are uniformly distributed throughout the material. It is also observed from Figure 9 (d-e), that carbon and boron are available in certain specific areas which represented their lower concentration in the sintered material and also, the formation of intermetallic carbide $(Fe,Cr)_{23}C_6$ and boride $(Cr,Fe)_2B$ phases.

Figure 10 is the SEM-SE image of S2-900 after exposure to a 3.5% NaCl solution for 27 h at different magnification. Figure 10(a) shows that uniform surface products were formed with some pyramid shaped, a black region where these surface products were absent. Figure 10(b-c) are images at higher magnification showing a more clear distribution of formed nano-sized surface products. In Figure 10(d), it was observed that these nano-sized surface products had rounded morphology and were agglomerated.

Figure 11(g-h) showed that the pyramid shape, that was found in Figure 10(a), consist of sodium and chlorine, which were distributed together in almost the same concentration. The observed pyramid shape could be a crystal of NaCl salt. The observation provides evidence that mainly, both elements were present in a chemical compound form on the surface of S2-900. It was also found that iron, chromium and molybdenum (which are the main alloying elements) are well distributed in S2-900.

On comparing the SEM analysis of both sintered samples as seen in Figure 6 and Figure 10, it was observed that a more uniform corrosion product was formed on S2-900 while in S1-800, a comparatively small area was covered with corrosion products. Similarly, the morphology of corrosion products was also different. By observing these results, it was concluded that the higher corrosion resistance of S2-900 is attributed to the formation of uniform surface products which are supposed to be the oxides of the alloying element. This observation also agreed with the literature [25].

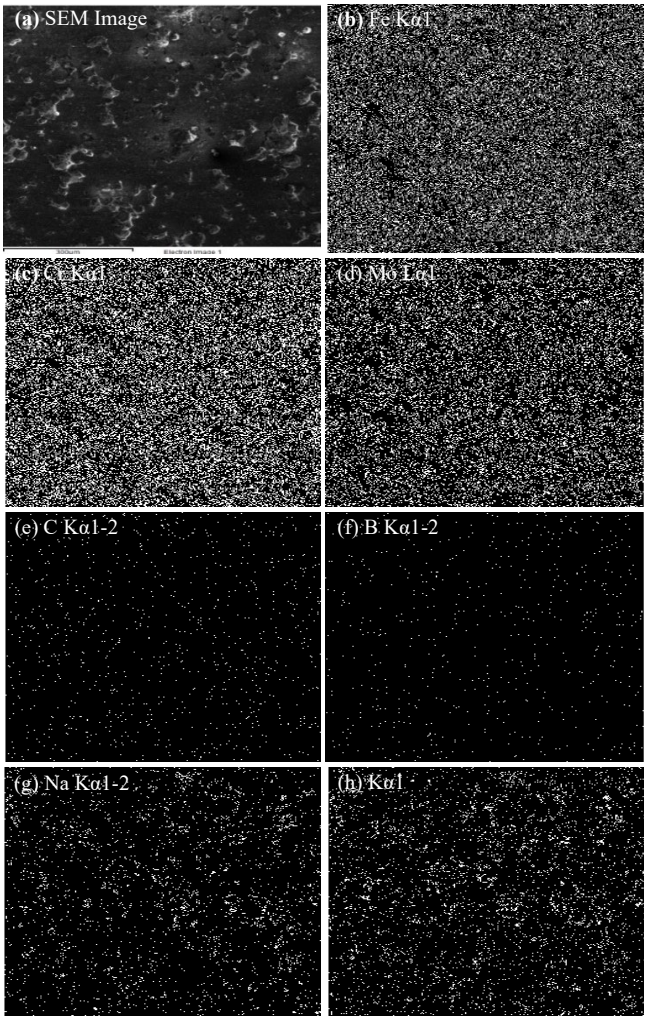

Figure 7. EDX-mapping analysis of S1-800 after exposing to a 3.5% NaCl solution for 27 h.

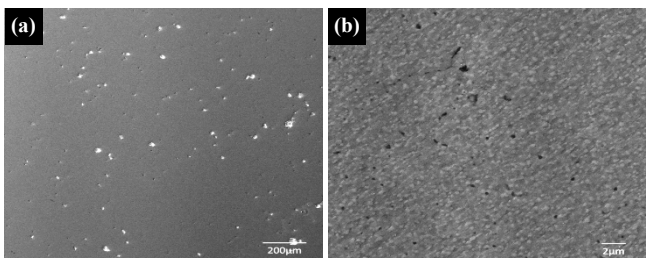

Figure 8. SEM-SE images of S2-900 before exposing to 3.5% NaCl solution, etched with 1 HCl : 3 HNO_3.

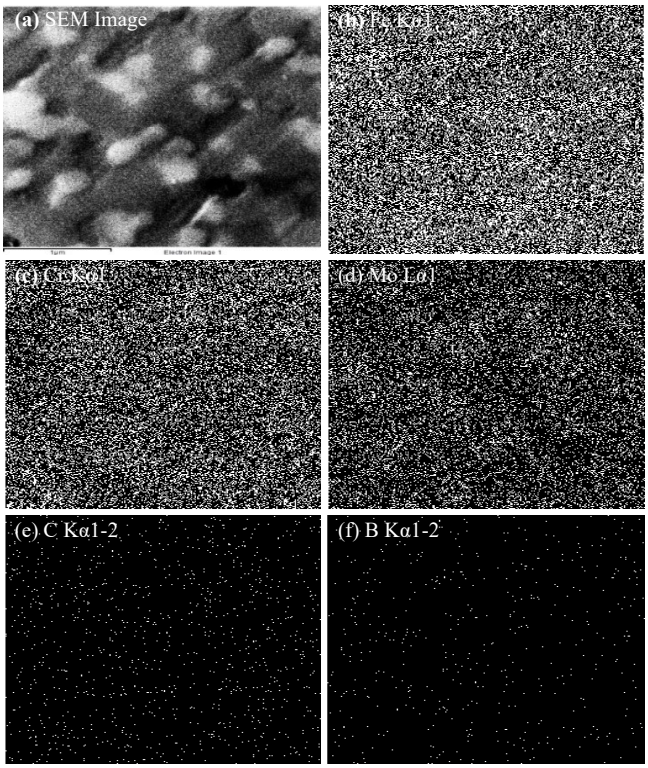

Figure 9. EDX-mapping analysis of S2-900 before exposing to a 3.5% NaCl solution.

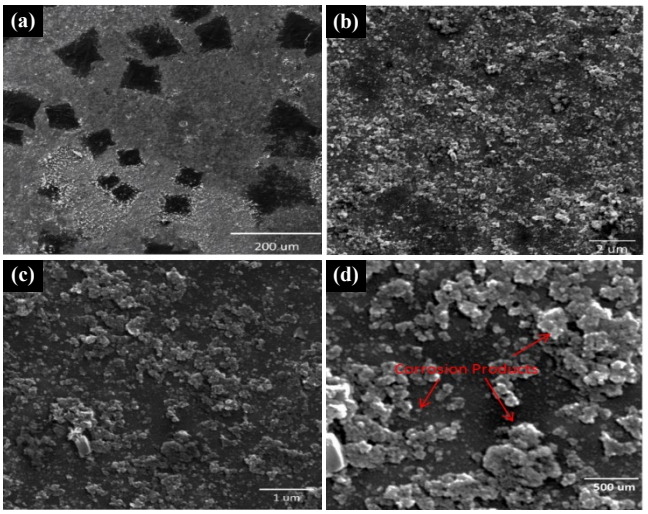

Figure 10. SEM-SE images of S2-900 after exposing to 3.5% NaCl solution for 27 h.

Figure 12 shows the XPS survey scan spectra of both samples after exposure to 3.5% NaCl solution for 27 h. It was observed that the detected elemental peaks in both samples were identical. However, the intensities were different which shows that the concentration of detected elements was not the same in the surface layer of both sintered samples. Figure 12(a, c) shows a survey scan spectra before argon etching. It was found that the concentration of oxygen in both samples was high as compared to other alloying elements, which is evidence of the formation of surface oxide. Figure 12(b, d) represents the survey scan spectra after mild argon etching. A clear decrease in the concentration of oxygen is observed in case of S-900, Figure 12(d). Similarly, it was observed that the concentration of other alloying elements increased which is the evidence of the oxide film removal due to argon etching. Also, the removal of the oxide layer from mild etching also showed that a thin oxide layer was formed. In S1-800, no considerable difference in oxygen concentration before and after argon etching was observed, Figure 12(a-b), which shows that a thicker oxide layer was formed as compared to S2-900.

The atomic percentage of alloying elements present at the surface and sub-surface of both sintered samples before exposing to 3.5% NaCl solution is represented in Figure 13. For the S1-800 sample, It is observed that the surface layer was enriched with iron and chromium while the contribution of molybdenum in oxide formation is much smaller. It is also observed that mild argon etching sharply decreased the atomic percentage of chromium while the percentage of iron and molybdenum were increased which indicates that the surface layer formed over S1-800 was actually enriched with chromium oxide. For the S2-900 sample, it is observed that the main contributor for surface layer formation is chromium, while the iron and molybdenum were also present in a significant amount. Furthermore, the mild argon etching decreased the atomic percentage of chromium and molybdenum both while the percentage of iron was increased. From these results, it is concluded that the chromium and molybdenum both were active in the formation of surface oxide over S2-900 samples while in the case of S1-800, the contribution of molybdenum in the formation of surface oxide was not significant

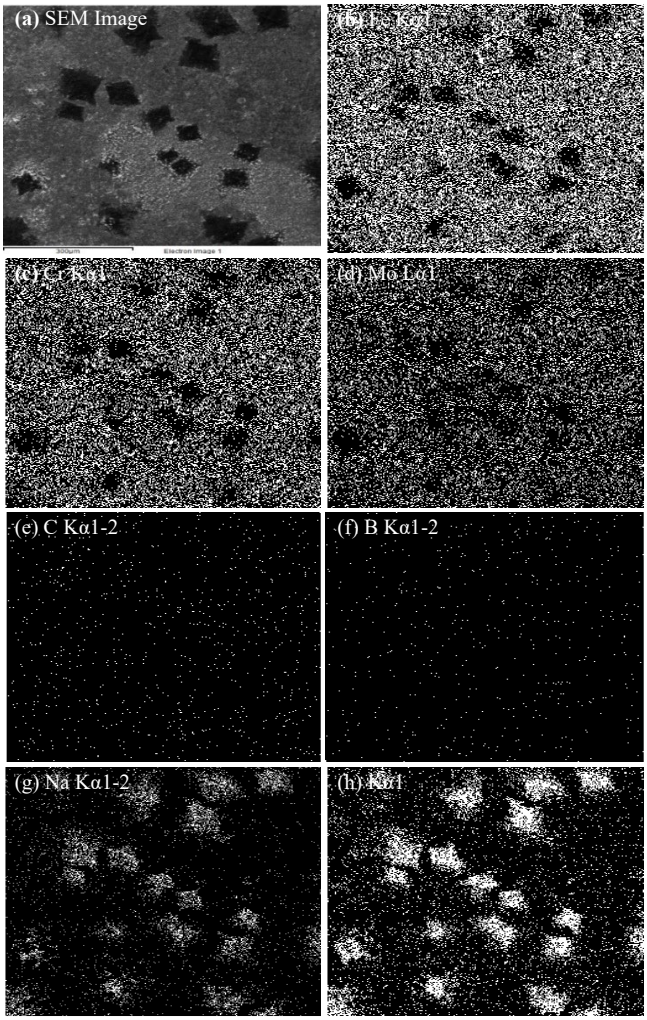

Figure 11. EDS-mapping analysis of S2-900 after exposing to a 3.5% NaCl solution for 27 h.

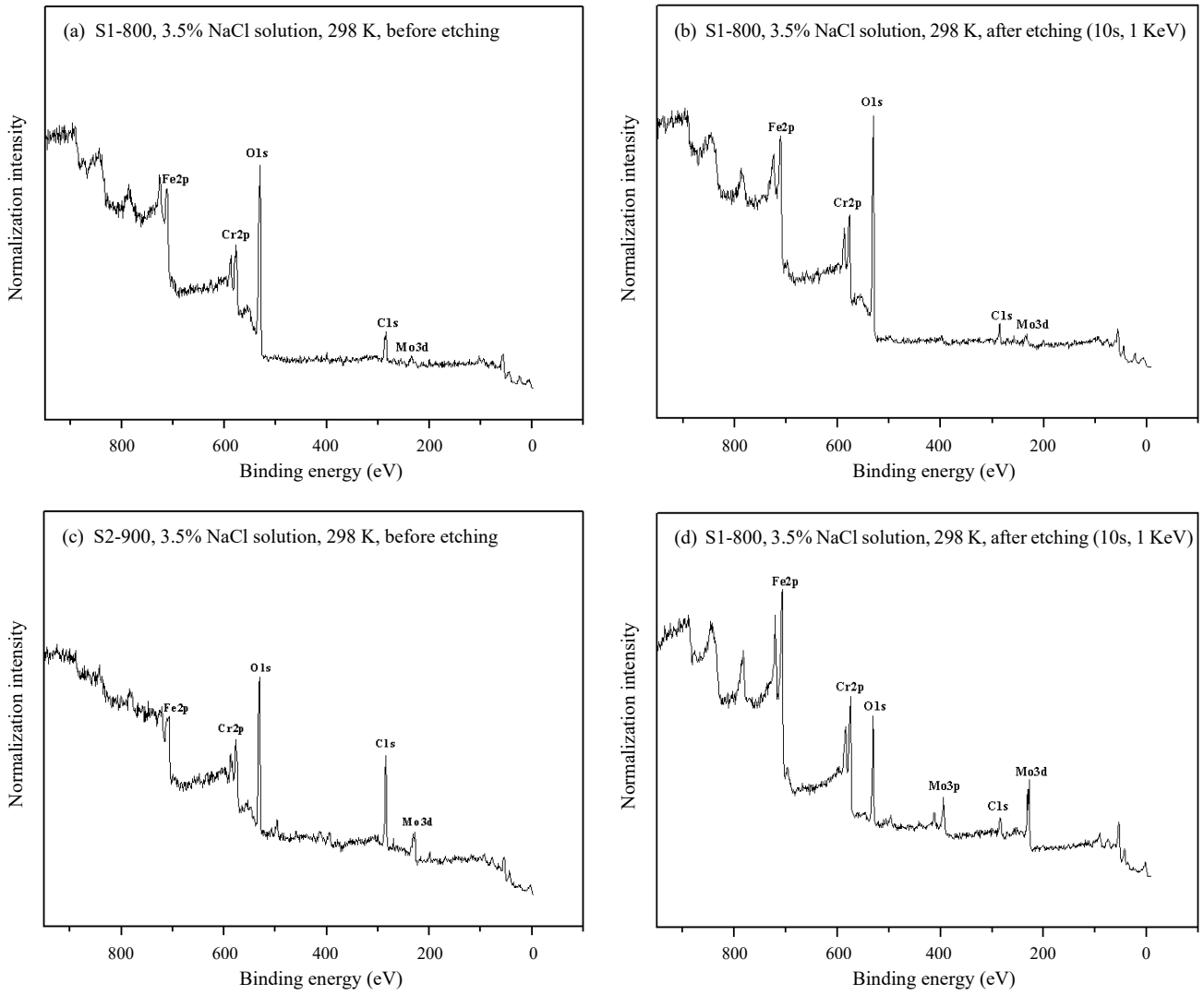

Figure 12. XPS survey scan spectra after immersing samples in 3.5% NaCl solution for 27 h.

Figure 14 shows a graphical representation of atomic percentages of alloying elements present at the surface and the sub-surface layer (after argon etching) of S1-800 and S2-900. It was observed that on both samples, iron was the main contributor for surface layer formation and the chromium was next to iron. A lesser amount of molybdenum, for both sintered samples, showed its weak contribution in surface layer formation. In S1-800, after mild argon etching, an 18% increase in the iron percentage and 15% decrease in chromium percentage was observed while the molybdenum percentage remained unaffected by etching. The appreciable depletion of chromium at sub-surface is evidence of a thick chromium oxide layer formation at the surface which got removed through argon etching. In contrast to S1-800, the S2-900 showed an opposite trend of 10% increase in chromium percentage with a 21% decrease in iron percentage. Also, the molybdenum percentage was increase from 2% before etching to 11 % after etching. Furthermore, the increase in iron percentage indicated that the iron has active contribution in surface layer formation.

Figure 15 represents the fitting of Fe2p, Cr2p and Mo3d core level spectra of both sintered samples. On the basis of binding energy, oxidation states of elements were determined. Figure 15(a-b) shows that the oxidation state of iron present in S1-800 were Fe(II) and Fe(III) while in S2-900, it was present as Fe^0 and Fe(III). From Figure 15(c-d), it was found that chromium was present as Cr(III) and Cr(VI) in S1-800 while in S2-900, the oxidation states were Cr^0 (metallic) and Cr(III). In Figure 15(e-f), it was observed that the oxidation state of molybdenum in S1-800 was Mo^0(metallic), Mo(V) and Mo(VI) while in S2-900, it was available as Mo^0(metallic), Mo(IV) and Mo(VI).

The characteristic binding energy of fitted peaks, the existing chemical state and the full width at half maximum (FWHM) values of fitted peaks are summarized in Table 5. The identified oxidation states are in well agreement with the literature [33-39]. It was observed that in S1-800, chromium ions form hydroxide ($Cr(OH)_3$) and hexavalent oxide (CrO_6) over the substrate which have limited protection against corrosion species attack as compared to chromium trivalent (Cr_2O_3) oxide. Also, no evidence of the formation of passive chromium trivalent oxide (Cr_2O_3) was detected in S1-800, which is one of the reasons for its weak corrosion resistance as observed in electrochemical testing.

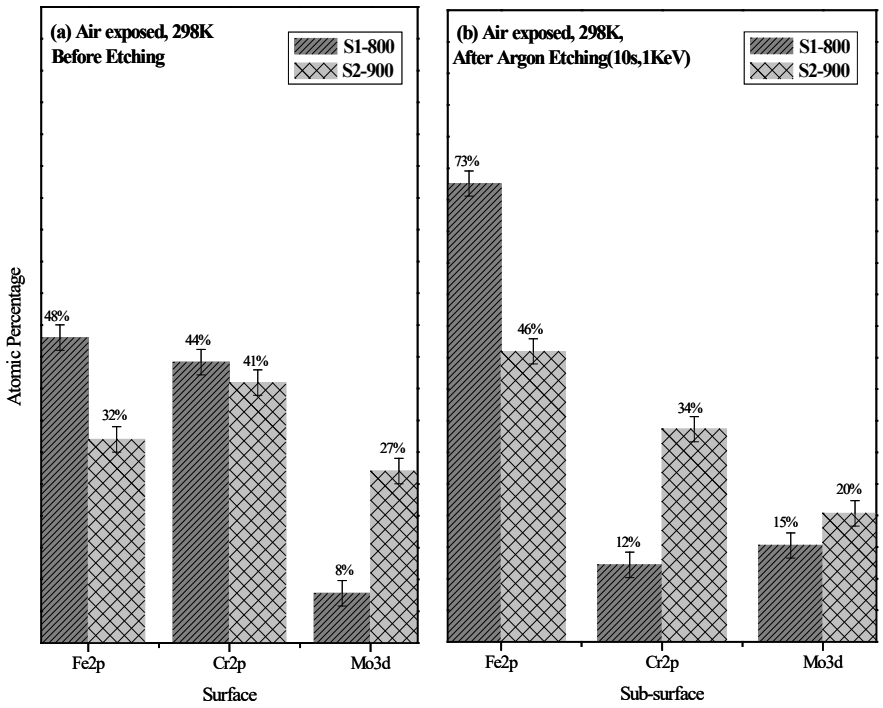

Figure 13. Atomic percentage of elements contribution in surface and sub-surface layer formation before exposing to 3.5% NaCl solution.

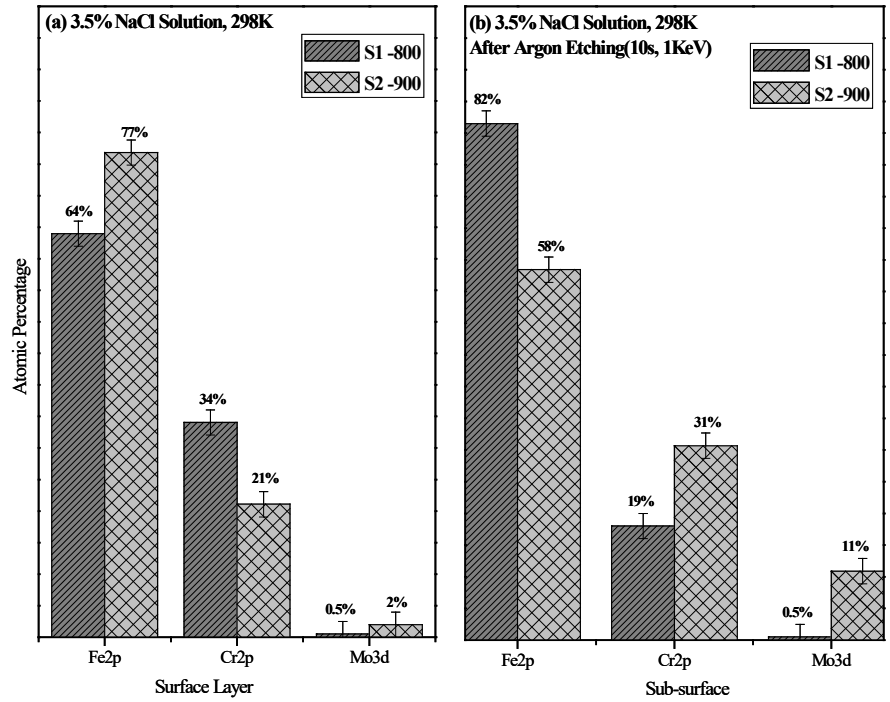

Figure 14. Atomic percentage of the elements contribution in surface layer formation when exposed to 3.5% NaCl solution for 27 h.

Figure 16 is a graphical representation of the alloying elements contribution in surface layer formation with existing oxidation states. It was found that the surface oxide formed on S1-800 was composed of more than half of iron oxides, one-third chromium oxides and a negligible amount of molybdenum oxides. The absence of metallic state indicated the formation of a thick oxide layer over S1-800 which reflects its poor corrosion resistance in exposed solution. It was observed that in S2-900, half of the detected oxidation states were a metallic state (i.e., Fe^0, Cr^0 and Mo^0) which showed the formation of a very thin protective oxide layer over the substrate, having dimensions less than the attenuation depth of XPS(~ 10 nm). The presence of the passive chromium oxide (Cr_2O_3) layer in S2-900 is responsible for the protective behavior, whereas the presence of Fe(III) oxidation state showed that some oxidation occurred at the surface. It was also observed that molybdenum contribution in S2-900 surface layer formation was less.

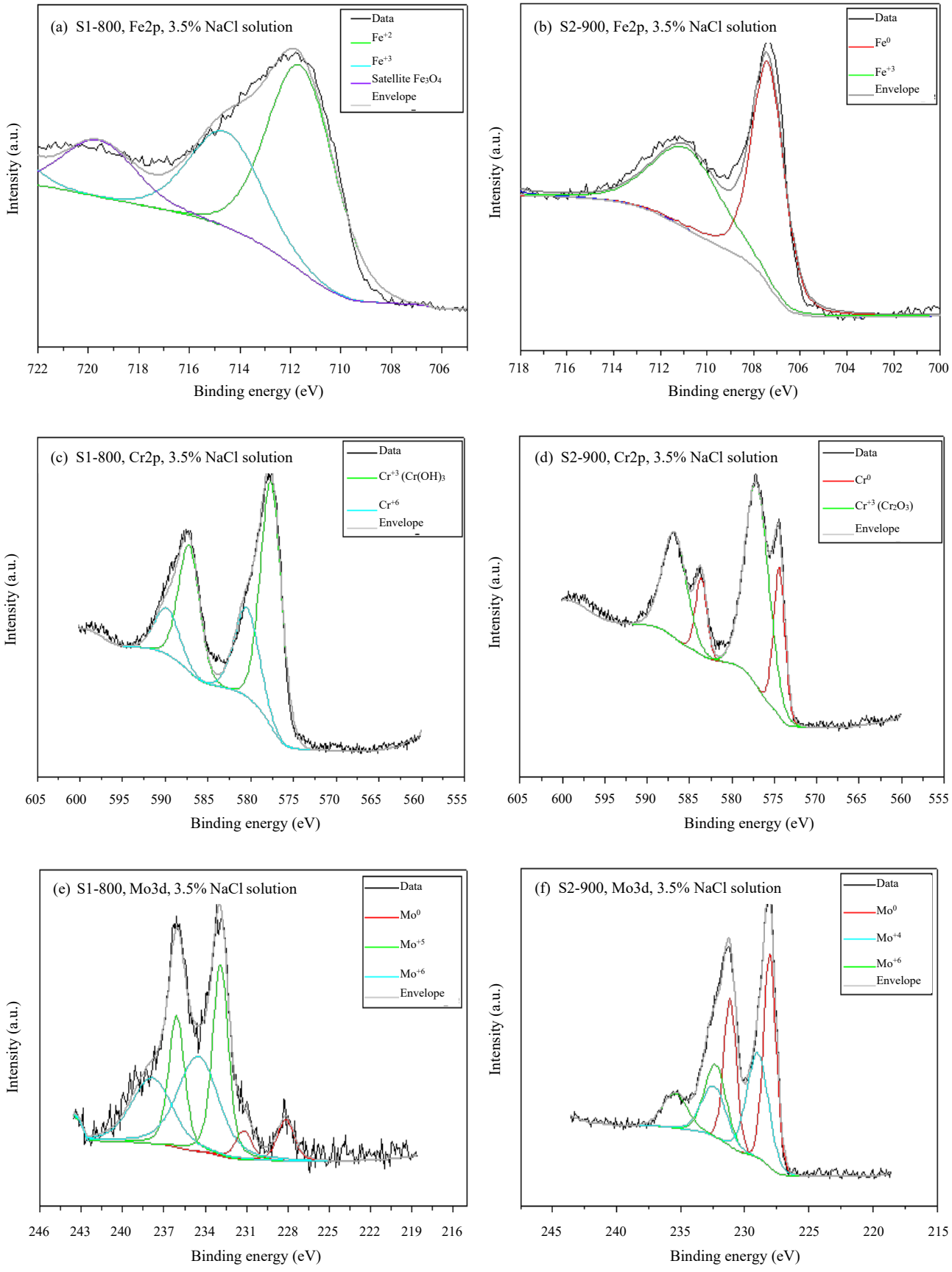

Figure 15. XPS analysis of Fe2p, Cr2p and Mo3d surface films formed after immersing samples in 3.5% NaCl solution for 27 .

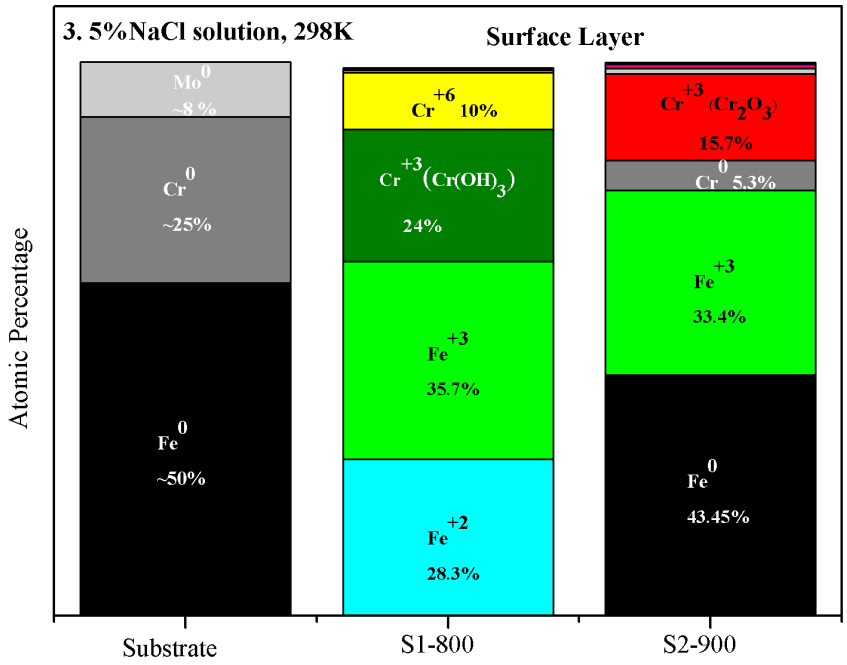

Figure 16. Atomic percentage of different oxidation states present at the surface layer after exposing to 3.5% NaCl solution for 27 h

Table 5. Summary of XPS analysis after exposing samples in 3.5%NaCl solution.

Spectra (3.5%NaCl)	Binding energy (eV)	FWHM (eV)	Chemical state	Relative atomic percentage (%) S1-800	Relative atomic percentage (%) S2-900
Fe2p3/2	706.70	1.64	Fe (metallic)	0.00	43.45
	710.80	3.37	Fe^{+3} (Fe_2O_3)	35.70	33.40
	714.37	3.37	Fe^{+2} – coexist with Fe^{+3}	28.30	0.00
	719.37	3.37	Magnetite(Fe_3O_4) representing satellite		0.00
Cr2p3/2	574.00	1.56	Cr (metallic)	0.00	5.30
	576.58	3.37	Cr^{+3} (Cr_2O_3)	0.00	15.70
	577.40	2.90	Cr^{+3} $Cr(OH)_3$	24.00	0.00
	580.25	3.37	Cr^{+6} (CrO_3)	10.00	0.00
Mo3d5/2	227.43	1.45	Mo (metallic)	< 2.00	< 2.00
	228.50	1.98	Mo^{+4} (MoO_4)	0.00	< 2.00
	232.08	1.37	Mo^{+5} ($MoCl_5$)	< 2.00	

4. Conclusions

The corrosion performance and mechanism of SPS sintered FeCrMo based alloy in 3.5% NaCl solution was analyzed through electrochemical laboratory techniques and x-ray photoelectron analysis. The electrochemical analysis shows that sintered samples are inferior to S.S-304 and better than CS-1080 conventional grade steel with respect to corrosion resistance performance. In comparison among sintered samples, S2-900 has better corrosion resistance performance than S1-800. XPS analysis shows that a protective thin chromium oxide layer (Cr_2O_3) was formed over S2-900 while on S1-800, a thick un-protective chromium hydroxide ($Cr(OH)_3$) and chromium-hexa-oxide (CrO_3) layer formation was detected. The main possible reasons for inferior corrosion performance of S1-800 as compared to S2-900 are; formation of non-uniform surface products and absence of passive chromium oxide (Cr_2O_3) on S1-800 surface.

Acknowledgements

This work was supported by King Fahd University of Petroleum and Minerals (KFUPM) under Grant #JF141007. We would like to acknowledge Liquid Metal Technologies, USA for providing initial amorphous powder.

References

[1] S. Pang, T. Zhang, K. Asami, and A. Inoue, "Effects of chromium on the glass formation and corrosion behavior of bulk glassy Fe-Cr-Mo-C-B Alloys.," *Materials Transactions*, vol. 43, no. 8, pp. 2137-2142, 2002.

[2] Z. M. Wang, Y. T. Ma, J. Zhang, W. L. Hou, X. C. Chang, and J. Q. Wang, "Influence of yttrium as a minority alloying element on the corrosion behavior in Fe-based bulk metallic glasses," *Electrochimica Acta*, vol. 54, no. 2, pp. 261-269, 2008.

[3] M. S. Bakare, K. T. Voisey, K. Chokethawai, and D. G. McCartney, "Corrosion behaviour of crystalline and amorphous forms of the glass forming alloy $Fe_{43}Cr_{16}Mo_{16}C_{15}B_{10}$," *Journal of Alloys and Compounds*, vol. 527, pp. 210-218, 2012.

[4] J. Jayaraj, Y. C. Kim, K. B. Kim, H. K. Seok, and E. Fleury, "Corrosion behaviors of $Fe_{45-x}Cr_{18}Mo_{14}C_{15}B_6Y_2M_x$ (M = Al, Co, Ni, N and x = 0, 2) bulk metallic glasses under conditions simulating fuel cell environment," *Journal of Alloys and Compounds*, vol. 434-435, no. SPEC. ISS., pp. 237-239, 2007.

[5] O. A. Graeve, R. Kanakala, L. Kaufman, K. Sinha, E.Wang, B. Pearson, G. Rojas-George, J. C. Farmer, "Spark plasma sintering of Fe-based structural amorphous metals (SAM) with Y_2O_3 nanoparticle additions," *Materials Letters*, vol. 62, no. 17-18, pp. 2988-2991, 2008.

[6] S. L. Wang, H. X. Li, X. F. Zhang, and S. Yi, "Effects of Cr contents in Fe-based bulk metallic glasses on the glass forming ability and the corrosion resistance," *Materials Chemistry and Physics*, vol. 113, no. 2-3, pp. 878-883, 2009.

[7] J. Eckert, J. Das, S. Pauly, and C. Duhamel, "Mechanical properties of bulk metallic glasses and composites," *Journal of Materials Research*, vol. 22, no. 02, pp. 285-301, 2007.

[8] S. Madge, "Toughness of bulk metallic glasses," *Metals*, vol. 5, no. 3, pp. 1279-1305, 2015.

[9] C. Suryanarayana, and A. Inoue, "Iron-based bulk metallic glasses," *International Materials Reviews*, vol. 58, no. 3, pp. 131-166, 2013.

[10] M. M. Trexler, and N. N. Thadhani, "Mechanical properties of bulk metallic glasses," *Progress in Materials Science*, vol. 55, no. 8, pp. 759-839, 2010.

[11] J. Jayaraj, K. B. Kim, H. S. Ahn, and E. Fleury, "Corrosion mechanism of N-containing Fe-Cr-Mo-Y-C-B bulk amorphous alloys in highly concentrated HCl solution," *Materials Science and Engineering A*, vol. 449-451, pp. 517-520, 2007.

[12] N. Chen, L. Martin, D. V. Luzguine-Luzgin, and A. Inoue, "Role of alloying additions in glass formation and properties of bulk metallic glasses," *Materials*, vol. 3, no. 12, pp. 5320-5339, 2010.

[13] A. Inoue, B. Shen, and A. Takeuchi, "Developments and applications of bulk glassy alloys in late transition metal base system," *Materials Transactions*, vol. 47, no. 5, pp. 1275-1285, 2006.

[14] J. Schroers, "Processing of bulk metallic glass," *Advanced Materials*, vol. 22, no. 14, pp. 1566-1597, 2010.

[15] S. F. Guo, K. C. Chan, S. H. Xie, P. Yu, Y. J. Huang, and H. J. Zhang, "Novel centimeter-sized Fe-based bulk metallic glass with high corrosion resistance in simulated acid rain and seawater," *Journal of Non-Crystalline Solids*, vol. 369, pp. 29-33, 2013.

[16] G. Kumar, A. Desai, and J. Schroers, "Bulk metallic glass: The smaller the better," *Advanced Materials*, vol. 23, no. 4, pp. 461-476, 2011.

[17] M. Park, *American Society for Metals Handbook Corrosion : Materials*, vol. 13. 2005.

[18] M. Ramya, S. G. Sarwat, V. Udhayabanu, S. Subramanian, B. Raj, and K. R. Ravi, "Role of partially amorphous structure and alloying elements on the corrosion behavior of Mg-Zn-Ca bulk metallic glass for biomedical applications," *Materials and Design*, vol. 86, pp. 829-835, 2015.

[19] A. Concustell, G. Alcala, S. Mato, T.G. Woodcock, A. Gebert, J. Eckert, and M.D. Baro, "Effect of relaxation and primary nanocrystallization on the mechanical properties of $Cu_{60}Zr_{22}Ti_{18}$ bulk metallic glass," *Intermetallics*, vol. 13, no. 11, pp. 1214-1219, 2005.

[20] K. Mondal, T. Ohkubo, T. Toyama, Y. Nagai, M. Hasegawa, and K. Hono, "The effect of nanocrystallization and free volume on the room temperature plasticity of Zr-based bulk metallic glasses," *Acta Materialia*, vol. 56, no. 18, pp. 5329-5339, 2008.

[21] J. Fornell, E. Rossinyol, S. Suriñach, M. D. Baró, W. H. Li, and J. Sort, "Enhanced mechanical properties in a Zr-based metallic glass caused by deformation-induced nanocrystallization," *Scripta Materialia*, vol. 62, no. 1, pp. 13-16, 2010.

[22] M. Chen, A. Inoue, W. Zhang, and T. Sakurai, "Extraordinary plasticity of ductile bulk metallic glasses," *Physical Review Letters*, vol. 96, no. 24, 2006.

[23] X. Li, H. Kato, K. Yubuta, A. Makino, and A. Inoue, "Improved plasticity of iron-based high-strength bulk metallic glasses by copper-induced nanocrystallization," *Journal of Non-Crystalline Solids*, vol. 357, no. 15, pp. 3002-3005, 2011.

[24] H. Y. Jung, and S. Yi, "Nanocrystallization and soft magnetic properties of $Fe_{23}M_6$ (M: C or B) phase in Fe-based bulk metallic glass," *Intermetallics*, vol. 49, pp. 18-22, 2014.

[25] L. Liu, Y. Li, and F. Wang, "Electrochemical corrosion behavior of nanocrystalline materials—a Review," *Journal of Materials Science and Technology*, vol. 26, no. 1, pp. 1-14, 2010.

[26] C. A. C. Souza, D. V Ribeiro, and C. S. Kiminami, "Corrosion resistance of Fe-Cr-based amorphous alloys : An overview," *Journal of Non-Crystalline Solids*, vol. 442, pp. 56-66, 2016.

[27] L. Wang, J. Zhang, and W. Jiang, "Recent development in reactive synthesis of nanostructured bulk materials by spark plasma sintering," *International Journal of Refractory Metals and Hard Materials*, vol. 39, pp. 103-112, 2013.

[28] F. Watari, A.Yokoyama, M. Omori, T. Hirai, H. Kondo, M. Uo, and T. Kawasaki, "Biocompatibility of materials and development to functionally graded implant for bio-medical application," *Composites Science and Technology*, vol. 64, no. 6, pp. 893-908, 2004.

[29] A. A. Sorour, M. Farooq, A. Mekki, and A. M. Kumar, "Corrosion of a spark plasma sintered Fe - Cr - Mo - B - C alloy in hydrochloric acid," *Metallography, Microstructure, and Analysis*, vol. 10, no. 3, pp. 291-301, 2021.

[30] D. Wallinder, J. Pan, C. Leygraf, and A. Delblanc-Bauer, "EIS and XPS study of surface modification of 316LVM stainless steel after passivation," *Corrosion Science*, vol. 41, no. 2, pp. 275-289, 1998.

[31] R. Solmaz, G. Kardaş, M. Çulha, B. Yazici, and M. Erbil, "Investigation of adsorption and inhibitive effect of 2-mercaptothiazoline on corrosion of mild steel in hydrochloric acid media," *Electrochimica Acta*, vol. 53, no. 20, pp. 5941-5952, 2008.

[32] E. McCafferty, *Introduction to Corrosion Science*, First. Springer, 2009.

[33] M. Vayer, I. Reynaud, and R. Erre, "XPS characterisations of passive films formed on martensitic stainless steel: qualitative and quantitative investigations," *Journal of Materials Science*, vol. 35, no. 10, pp. 2581-2587, 2000.

[34] S. D. Zhang, J. Wu, W. B. Qi, and J. Q. Wang, "Effect of porosity defects on the long-term corrosion behaviour of Fe-based amorphous alloy coated mild steel," *Corrosion Science*, vol. 110, pp. 57-70, 2016.

[35] D. S. Petrovič, and D. Mandrino, "XPS characterization of the oxide scale on fully processed non-oriented electrical steel sheet," *Materials Characterization*, vol. 62, no. 5, pp. 503-508, 2011.

[36] T. Yamashita, and P. Hayes, "Analysis of XPS spectra of Fe^{2+} and Fe^{3+} ions in oxide materials," *Applied Surface Science*, vol. 254, no. 8, pp. 2441-2449, 2008.

[37] X. Y. Li, E. Akiyama, H. Habazaki, A. Kawashima, K. Asami, and K. Hashimoto, "Electrochemical and XPS studies of the corrosion behavior of sputter-deposited amorphous Fe-Cr-Ni-Nb alloys in 6 M HCl," *Corrosion Science*, vol. 41, no. 6, pp. 1095-1118, 1999.

[38] M.-D. N., P. M. A. Galtayries, and R. Warocquier-Cle′ rout, "Fibronectin adsorption on Fe–Cr alloy studied by XPS," *Surface and Interface Analysis*, vol. 38, pp. 186-190, 2006.

[39] C. O. A. Olsson, H. J. Mathieu, and D. Landolt, "Angle-resolved XPS analysis of molybdenum and tungsten in passive films on stainless steel PVD alloys," *Surface and Interface Analysis*, vol. 34, no. 1, pp. 130-134, 2002.